Free Piston Stirling Engine as a new heat recovery option for an Internal Reforming Solid Oxide Fuel Cell

Mahdi Majidniya, Benjamin Rémy, Thierry Boileau, Majid Zandi

Free Piston Stirling Engine as a new heat recovery option for an Internal Reforming Solid Oxide Fuel Cell

Mahdi MAJIDNIYA[1*], Benjamin REMY[1], Thierry BOILEAU[1], Majid ZANDI[2]

[1]Université de Lorraine, CNRS, LEMTA
F-54000 Nancy, France
[2] Renewable Energies Engineering Department, Shahid Beheshti University
Tehran, Iran
[*](Corresponding author: Mahdi.Majidniya@univ-lorraine.fr)

Abstract – Energy demand increment besides the reduction of fossil fuel resources from one side, and climate issues concerning the conventional power production methods from another side lead humanity to more efficient and cleaner power production methods. One of these methods is polygeneration microgrids based on a renewable energy source. In the present study, a combined cycle of a Free Piston Stirling Engine with a Permanent Magnet Linear Synchronous Machine was proposed as a new heat recovery option for the high-quality thermal energy of an Internal Reforming Solid Oxide Fuel Cell as electricity. Then, a Double Effect Absorption Chiller and a heat exchanger were used to recover the rest of the heat as cooling and hot water, respectively. After modeling and validating all the systems, they were combined. The results of the combined system showed 31.7% (or 40% by including cooling production of Double Effect Absorption Chiller instead of its heat consumption for efficiency calculation) of total efficiency improvement compared to the standalone Internal Reforming Solid Oxide Fuel Cell. Furthermore, the electrical efficiency of the system was improved by 14.1%.

Keywords: Free Piston Stirling Engine (FPSE); Permanent Magnet Linear Synchronous Machine (PMLSM); Internal Reforming Solid Oxide Fuel Cell (IRSOFC); Double Effect Absorption Chiller (DEACH); Waste heat recovery; Microgrid

Graphical Abstract

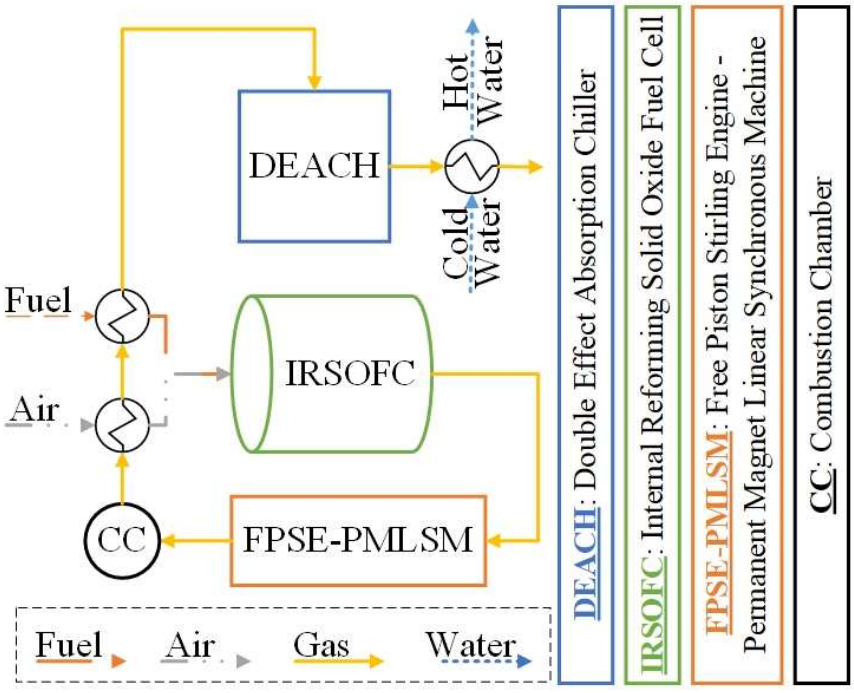

Nomenclature

A	Area, m^2
$a; b; c$	Reaction extents, mol/s
$\underline{A}; \underline{B}; \underline{C}; \underline{D}; \underline{E}$	Constants
B_v	Friction coefficient
C	Clearance, m
C_f	Darcy friction factor
Cp	Heat transfer coefficient at constant pressure, J/(kgK)

Greek symbols

γ	Specific heat ratio
ΔG	Gibbs free energy changes, J/mol
η	Efficiency
$\theta; \phi$	Angle
Υ	Pre-exponential factor, A/m^2
ρ	Density, kg/m3

Cv	Heat transfer coefficient at constant volume, J/(kgK)
d	Diameter, m
E	Energy, J/kg
F	Force, N
Fr	Faraday constant, 96487 C/mol
h	Convective heat transfer coefficient, W/(m^{2}K)
H	Enthalpy (J/kg)
i	Current, A; Current density, A/m^2
i_0	Exchange current density, A/m2
i_l	Limiting current density, A/m2
K	Reaction equilibrium constant
L	Inductance, mH, Length, m
LHV	Lower Heating Value, J/kg
l	Length, m
$M; m$	Mass, kg
$\dot{n}_j^i$	Molar flow rate of component i in channel j, mol/s
n_e	Number of electrons
P	Pressure, Pa
$\dot{Q}$	Heat transfer rate, W
Q_{rxn}	Reaction heat, J
R	Gas constant
r	Resistance, Ω
Re	Recirculation ratio
S	Entropy, J/K
T	Temperature, K
u	Velocity, m/s
U_f	Fuel utilization factor
U_{ox}	Air utilization factor
V	Volume, m^3
v	Voltage, V
X^i	Molar concentration of component i
x	Displacement, m
ψ_f	Flux linkage, Wb
ω	Frequency, rad/s

Index and exponent

0	Standard state
Act	Activation
An	Anode
b	Buffer
c	Compression
Ca	Cathode
Con	Concentration
D	Displacer
$d; q$	Axis
e	Expansion
el	Electric
em	Electromagnetic
eq	Equilibrium
gs	Gas spring
h	Heater
k	Cooler
l	Limiting
m	Mover
Ohm	Ohmic
p	Power piston
pr	Product
R	Regenerator
r	Reforming
re	Reactant
rev	Reversible
s	Shifting
w	Wire

Abbreviation

FPSE	Free Piston Stirling Engine

$\dot{x}$	Velocity, m/s	PMLSM	Permanent Magnet Linear Synchronous Machine
$\ddot{x}$	Acceleration, m/s^2	IRSOFC	Internal Reforming Solid Oxide Fuel Cell
Xm	Mass concentration	DEACH	Double Effect Absorption Chiller

1. Introduction

Reduction of fossil fuel resources, on the one hand, and increasing the energy demand, on the other hand, create a big concern about the future of the world energy supply. Adding climate changes to these issues cause much attention to be drawn to an alternative clean and efficient power production source. Nowadays, most of the required power is produced by centralized power plants, which generally have a low efficiency at 30-40%. The results of such a low efficient system are high running costs, high waste of energy, and also many CO_2 productions. The solution to this problem is moving from centralized power production systems to the high efficient and clean microgrids [1].

Recently, fuel cells attract much attention as the primary power source for microgrids [2]. These systems have higher efficiency compared to internal combustion engines and coal-fired power plants. Also, since fuel cells do not have any moving parts, they have silent and reliable operation. Furthermore, for combined heat and power systems, the exhaust heat of the high-temperature fuel cells can be used. Also, virtually there is no SO_x, NO_x, and particulate emissions [3,4].

Coupling the high-temperature fuel cells with heat recovery systems improves the performance of the system. One of the interesting methods to recover this heat is using Stirling engines due to their high efficiency and high potential to reduce overall costs [5]. Furthermore, Stirling engines, because of their external combustions, can be coupled with different systems like solar energy-based systems [6], gasification systems [7], external combustion chambers [8], and high-temperature fuel cells [9]. Stirling engines, compared to conventional systems, like gas turbines, that can be used beside the high-temperature fuel cells, have a silent operation. Another advantage is that conventional heat recovery systems, like gas turbines, generally require high-pressure fuel cells. However, by using Stirling engines, the fuel cell can work at atmospheric pressure [10]. Furthermore, a Stirling engine combined with a fuel cell is more adapted for variable energy demands than a gas turbine or an organic Rankine cycle [11]. These features encouraged researchers to study the combination of the fuel cell with a Stirling engine.

Obara et al. [12] have studied the combination of a Woody Biomass Stirling Engine with a Proton Exchange Membrane Fuel Cell. They have used the exhaust high-temperature gases of the Stirling engine for the reforming of the fuel cell. Their goal of this combination has been to improve the exergy efficiency of the Woody Biomass Stirling Engine. Sánchez et al. [10] have used an externally fired - Stirling - piston engine instead of the conventional gas turbine system combined with a fuel cell. They have compared the Stirling engine's combination with Molten Carbonate Fuel Cell with two other commonly used systems for fuel cell heat recovery. They have shown that the combined system's performance with the Stirling engine has been better than other systems. They have confirmed that the benefit of using the Stirling engine has not been just efficiency improvement. Using Stirling engines has made it possible to use fuel cells in the coupled mode at atmospheric pressure and disconnect the Stirling engine from the fuel cell system to operate in standalone mode. Rokni [13] has analyzed a combined cycle of a SOFC

with a Stirling engine. He has been able to improve the efficiency of the combined system compared to standalone systems. The power generation of the combined system compared to the SOFC standalone system has been increased by 10%. The efficiency of the combined system has also been about 60%. He has continued his work on this topic with different system combinations [9,14,15]. Escalona et al. [16] have studied the combination of a Molten Carbonate Fuel Cell with two closed systems: a Stirling engine and a carbon dioxide turbine. They have compared both systems' results and finally have concluded that these systems have had better performance compared to the high-pressure fuel cells combined with a gas turbine. Chen et al. [17] have also analyzed a combined system of a Molten Carbonate Fuel Cell with a Stirling engine. They have shown that the performance of the Molten Carbonate Fuel Cell has been greatly improved when it has been combined with the Stirling engine. They have also studied the effect of multiple irreversible losses and different operating conditions like operating temperature and pressure on the system. Mehrpooya et al. [18] have analyzed a combined system of a Molten Carbonate Fuel Cell, a Stirling engine, and a double-effect absorption chiller. They have done an energy and exergy analysis of the system. The overall and electrical efficiency of the system have been 71.71% and 42.28%, respectively. Hosseinpour et al. [19] have also studied a combined system of a SOFC with a Stirling engine. They have studied the effect of current density, SOFC inlet temperature, compression ratio, and regenerator effectiveness on system performance. The efficiency of the combined system has been around 24% more than the SOFC standalone system. The results have also revealed that the SOFC inlet temperature increment to a certain value has increased the combined system's exergy efficiency. Ansarinasab et al. [20] have studied a combined system of a Molten Carbonate Fuel Cell, a Stirling engine, and a gas turbine to produce heating, cooling, and electricity. For cooling, a double-effect absorption chiller has been used. They have done an exergy cost analysis on the system. Habibollahzade et al. [21] have compared three systems from energy, exergy, exergoeconomic, and environmental perspectives. The first system has been a SOFC. The second one has been a SOFC combined with a Stirling engine. The third system has been a SOFC combined with a Stirling engine that the surplus power of the SOFC has been used in a proton exchange membrane electrolyzer to produce hydrogen. From all points of view, SOFC combined system with a Stirling engine has been the best system. Luo et al. [11] have studied a combined cooling and power generation system based on four power systems: SOFC, SOFC-gas turbine, SOFC-Stirling engine, and SOFC-organic Rankine cycle. The effect of some parameters like fuel inlet temperature, SOFC current density, and gas turbine pressure ratio on the system has been studied. For constant energy demand, the SOFC-gas turbine system has been recommended, while for the variable energy demand of the building, the SOFC-Stirling engine system has been suggested. Marefati et al. [22] have analyzed a combined system of a SOFC, a Stirling engine, a steam turbine, a linear Fresnel solar field, and a double effect absorption chiller to produce electricity, heating, and cooling. The electrical, energy, and exergy efficiencies of the system have been 49.7%, 67.5%, and 55.6%, respectively. Also, a sensitivity analysis of the system has been done. Salehi et al. [23] have studied and compared three different systems coupled with a biomass gasifier: Molten Carbonate Fuel Cell system, Molten Carbonate Fuel Cell with Stirling engine, and Molten Carbonate Fuel Cell with Stirling engine and Rankine cycle. Energetic, exergetic, and environmental analyses have been done on the systems. The maximum efficiency of the whole combined system has been 28.4% more than the Molten Carbonate Fuel Cell standalone system. Moradpoor et al. [24] have analyzed a combined system of a Molten Carbonate Fuel Cell, Stirling engine, absorption chiller, and Kalina power generation cycle. They have also done a parametric and sensitive analysis. The results have shown that this system has saved up to 45% of fuel than a conventional system. The overall and electrical efficiencies of this system have been 70% and 50%, respectively. Moradi et al. [25] have studied a combined cycle of a SOFC

with a multi-effect desalination system and a Stirling engine. They have shown that the combined system has had 11.7% higher efficiency compared to the same system but in the absence of the Stirling engine.

As can be seen, the Stirling engine has been used as a heat recovery option for different types of fuel cells. For the present study, an IRSOFC is chosen as the main power production source. SOFC, compared to other fuel cells, has the advantage that can work with a wide range of fuels [26,27], including methane [28], ethanol [29], carbon [30], syngas, hydrogen [31], biogenous fuels such as biogas [32], and so on. However, for some types of fuels, there might be some constraints and considerations related to trace contaminants [33,34]. The ability to work with different fuels makes it possible for SOFC to handle fluctuations of fuel compositions or fuel type change [35]. Also, compared to most other types of fuel cells, SOFC produces a high amount of exhaust heat, which is useful for combined systems, specially multigeneration ones [4].

Stirling engines also can be classified into different categories. From the energy conversion point of view, they can be classified into standard Stirling engines and Free Piston Stirling Engines (FPSE). Standard Stirling engines convert the linear movement of the piston to a rotary one through a crankshaft to produce electricity by a rotary generator. FPSEs directly use the linear movement of the piston in a linear generator to produce electricity. FPSEs are more compact and lightweight than standard Stirling engines, and also, due to the better sealing, they can keep working gasses for more working cycles inside them [36,37]. Such aspects make FPSE combined with a linear generator a perfect choice for the heat recovery of microgrids. Also, for the linear generator, a three-phase Permanent Magnet Linear Synchronous Machine (PMLSM) is used. A three-phase machine needs less wire compared to an equivalent one-phase one, and also, a permanent magnet generator has higher efficiency compared to an induction one [38,39].

Thus, an FPSE-PMLSM system is used to recover the high-quality thermal energy of the exhaust gasses of the IRSOFC. Then, a double-effect absorption chiller and a heat exchanger are used to recover the rest of the thermal energy in the forms of cooling and heating, respectively.

The most important point which makes the current study original, and has not been already done, is using a Free Piston Stirling Engine combined with a Permanent Magnet Linear Synchronous Machine (FPSE-PMLSM) as a waste heat recovery option for a Fuel Cell. Considering the advantages of Solid Oxide Fuel Cell (SOFC) and FPSE-PMLSM (that were already discussed in detail) makes them a great candidate for distributed power generation systems. These interesting aspects of both systems encouraged the authors to study their combination in such a newly developed trigeneration configuration. The detailed modeling of the systems, especially the FPSE-PMLSM one that a precise thermo-dynamic and electric model of it was developed, is another strength of the present study that has not been done before in such a combination. Providing only a thermic model of the FPSE-PMLSM system and ignoring the electric and thermodynamic model as done by many researchers and explained in [40,41] may cause a loss of precision, leading to unrealistic performance estimation.

In the present study, at first, an IRSOFC was modeled and validated. In the next step, a nonlinear thermodynamic model of an FPSE was presented. This model could predict the behavior of the system in dynamic conditions. After FPSE validation, a PMLSM was modeled as its generator. Then, FPSE was coupled with PMLSM, and the combined system was controlled. After that, a Double Effect Absorption Chiller (DEACH) was modeled and validated. Since there was no need to have a high-pressure fuel cell, the IRSOFC in the combined system worked at atmospheric pressure. Since electricity production was the main interest of the proposed combined system which is a part of a microgrid, to recover the high-

quality heat of the IRSOFC, the FPSE-PMLSM system was put before the IRSOFC gas/air preheaters. Finally, the results of the whole combined system were presented in the last section.

2. System Description

In Figure 1, the schematic of the combined system is shown. At first, air and fuel are fed to IRSOFC ① to produce electricity. The exhaust gas of the Internal Reforming Solid Oxide Fuel Cell (IRSOFC) ② has a high temperature that is used in a Free Piston Stirling Engine combined with a Permanent Magnet Linear Synchronous Machine (FPSE-PMLSM) to produce electricity. Then, the gas leaves the FPSE-PMLSM system ③ with a decreased temperature. Since this gas still contains burnable substances, a Combustion Chamber (CC) is used to burn them and increase the gas temperature ④. Then, this gas passes through a heat exchanger ⑤ to preheat the input air ⑥. After that, it passes through another heat exchanger ⑦ to preheat the input fuel ⑧. This gas still has enough energy to run a Double Effect Absorption Chiller (DEACH) ⑨. The final low-quality thermal energy heats the water ⑩ and provides hot water.

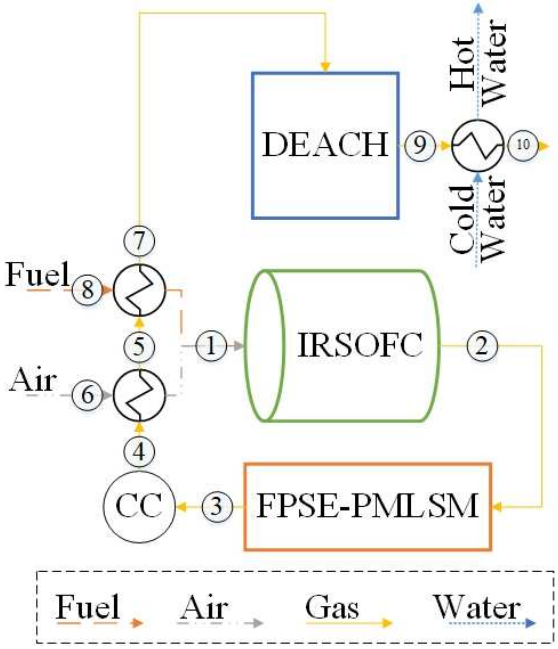

Figure 1: Combined system schematic

3. IRSOFC Analysis

Here a zero-dimensional model of IRSOFC is developed. The following assumptions are made to model the IRSOFC system:

- The IRSOFC operates at a steady-state
- The IRSOFC is isolated and has no heat transfer with the environment
- It is a tubular IRSOFC
- The radiation heat transfer between solid structure and gas channels is ignored
- The contact resistances are ignored

3.1. Internal Reformer

An internal reformer, compared to an external one, has higher efficiency and lower cost [42]; thus, an internal reformer was chosen. The three main reactions that happen inside the reformer are:

$$a \Longrightarrow CH_4 + H_2O \longrightarrow CO + 3H_2 \quad (1)$$

$$b \Longrightarrow CO + H_2O \longrightarrow CO_2 + H_2 \quad (2)$$

$$c \Longrightarrow H_2 + 1/2\ O_2 \longrightarrow H_2O \quad (3)$$

In these equations, a, b, and c are extents of reforming, shifting, and electrochemical reactions (mol/s), respectively. The equilibrium constants of reforming (r subscript-eq (1)) and shifting (s subscript- eq(2)) reactions can be calculated based on partial pressures of gasses in the reactions which are related to their equilibrium molar concentrations:

$$K_r = (P^{CO}(P^{H_2})^3)/(P^{CH_4}P^{H_2O}) = \left(X_{eq}^{CO}\left(X_{eq}^{H_2}\right)^3\right)/\left(X_{eq}^{CH_4}X_{eq}^{H_2O}\right) \times (P/P_0)^2 \quad (4)$$

$$K_s = (P^{CO_2}P^{H_2})/(P^{CO}P^{H_2O}) = \left(X_{eq}^{CO_2}X_{eq}^{H_2}\right)/\left(X_{eq}^{CO}X_{eq}^{H_2O}\right) \quad (5)$$

These coefficients are also a function of temperature:

$$\ln K = \underline{A}T^4 + \underline{B}T^3 + \underline{C}T^2 + \underline{D}T + \underline{E} \quad (6)$$

$\underline{A}$, $\underline{B}$, $\underline{C}$, $\underline{D}$, and $\underline{E}$ are constants, and their values are presented in Table 1.

Table 1: Constants to calculate equilibrium constants of equations [43]

	Reforming (for K_r)	Shifting (for K_s)
$\underline{A}$	-2.63121×10^{-11}	5.47301×10^{-12}
$\underline{B}$	1.24065×10^{-7}	-2.57479×10^{-8}
$\underline{C}$	-2.25232×10^{-4}	4.63742×10^{-5}
$\underline{D}$	1.95028×10^{-1}	-3.91500×10^{-2}
$\underline{E}$	-6.61395×10	1.32097×10

Since in equation (4) and (5), partial gas pressures are related to their equilibrium molar concentrations, and these equations are rewritten based on equilibrium molar concentrations, the first step to model the reformer is to calculate gas compositions at different channels of Figure 2. Since the chemical reactions in the anode need water as a reactant, and the output gas mixtures of the anode ($An4$) has high water content, the fuel ($An1$) before entering the anode mixes with the recirculated gas mixture ($An2$). Also, the oxidant is fed to cathode ($Ca1$).

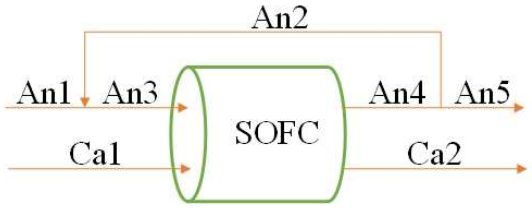

Figure 2: SOFC flow channels

Based on Figure 2, the molar gas flow rate for $An3$ and $An4$ for each gas (i) can be calculated as [44]:

$$\dot{n}_{An3}^i = \dot{n}_{An1}^i + \dot{n}_{An2}^i = \dot{n}_{An1}^i + X_{eq}^i \dot{n}_{An2} = \dot{n}_{An1}^i + X_{eq}^i(Re\dot{n}_{An4}) \quad (7)$$

$$\dot{n}_{An4}^i = \dot{n}_{An3}^i + d^i \rightarrow \dot{n}_{An4} = \dot{n}_{An3} + 2a \quad (8)$$

Here $\dot{n}_j^i$ is the molar flow rate of component i in channel j and $\dot{n}_j$ is the total molar flow rate in channel j. The values of d^i based on a, b, and c are given in Table 2.

Table 2: d^i values to calculate An4 gas flow rates [44]

d^{CH_4}	$-a$	d^{CO_2}	b
d^{H_2O}	$-a-b+c$	d^{H_2}	$3a+b-c$
d^{CO}	$a-b$	d^{N_2}	0

Thus, the total gas flow rate in $An3$ is [44]:

$$\dot{n}_{An3} = (\dot{n}_{An1} + 2aRe)/(1-Re) \tag{9}$$

Re is the recirculation ratio that here is assumed to be equal to 0.6. Combination of equations (7) - (8) allows calculating the equilibrium gas molar composition in $An4$ Channel [44]:

$$X_{eq}^i = \left(\dot{n}_{An4}^i\right)/(\dot{n}_{An4}) = \left(\dot{n}_{An1}^i + d^i\right)/(\dot{n}_{An1} + 2a) \tag{10}$$

For CH_4, CO_2, CO, and N_2, the d^i values are based on Table 2, and for H_2O and H_2 the equilibrium gas molar compositions in $An4$ are as [44]:

$$X_{eq}^{H_2} = \left(\dot{n}_{An1}^{H_2} + 3a + b\right)/(\dot{n}_{An1} + 2a) \times \left((1-Re)\left(1-U_f\right)\right)/\left(1-Re+ReU_f\right) \tag{11}$$

$$X_{eq}^{H_2O} = \left(\dot{n}_{An1}^{H_2O} + \left(-a-b+U_f\left(\dot{n}_{An1}^{H_2} + 3a + b\right)/\left(1-Re+ReU_f\right)\right)\right)/(\dot{n}_{An1} + 2a) \tag{12}$$

U_f in these equations is the fuel utilization factor, which is assumed to be equal to 0.85. For the cathode side (air channel), gases molar flow rates and equilibrium gases molar compositions are as [44]:

$$\dot{n}_{Ca1}^{O_2} = c/(2U_{ox}) \tag{13}$$

$$\dot{n}_{Ca1}^{N_2} = c/(2U_{ox}) \times 79/21 \tag{14}$$

$$\dot{n}_{Ca2}^{O_2} = c/(2U_{ox}) - c/2 \tag{15}$$

$$\dot{n}_{Ca2}^{N_2} = c/(2U_{ox}) \times 79/21 \tag{16}$$

Here U_{ox} is the air utilization factor, which is assumed to be 0.25. The unknown variables of these equations are a, b, and total mass flow rate in $An1$. These variables can be found by solving the equations (4), (5), and the following equation (17) at the same time [44]:

$$i_{cell}A_{cell} = 2cFr = 2\left(\left(\left(\dot{n}_{An1}^{H_2} + 3a + b\right)U_f\right)/\left(1-Re+ReU_f\right)\right)Fr \tag{17}$$

Unknown parameters of these equations are a, b and fuel flow rate ($\dot{m}_{fuel}$) which is needed to calculate $\dot{n}_{An1}^i$. Since c can be calculated based on a and b, it is not an independent parameter. The flow chart of the internal reformer modeling procedure is shown in Figure 3.

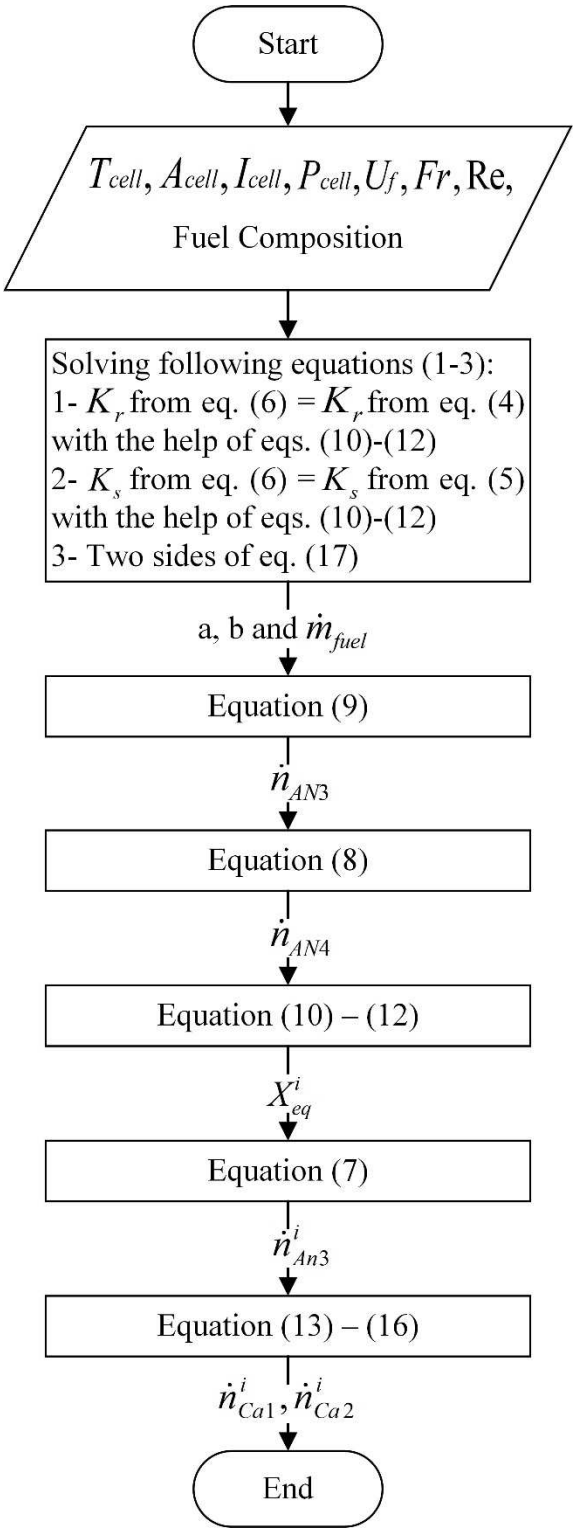

Figure 3: Internal reformer flow chart

3.2. SOFC Voltage

The reversible voltage of the cell can be calculated based on the Nernst equation [45]:

$$v_{rev} = v_0 + \Delta v = -\Delta G_0/(n_e Fr) - \Delta G/(n_e Fr) = -\Delta G_0/(2Fr) + (RT)/(2Fr)\ln(P^{H_2}(P^{O_2})^{0.5}/P^{H_2O}) \quad (18)$$

n_e is the number of electrons that here is equal to 2. Partial pressures of gasses are related to their molar concentrations in $An4$ that were already calculated in section 3.1. Due to irreversibilities, the actual voltage is smaller than this value and is equal to [45]:

$$v = v_{rev} - (v_{Act} + v_{Ohm} + v_{Conc}) \tag{19}$$

As can be seen, there are three different polarization types: activation (Act subscription), ohmic (Ohm subscription), and concentration ($Conc$ subscription). Activation polarization can be calculated as [43]:

$$\begin{aligned} v_{Act} &= v_{Act,An} + v_{Act,Ca} \\ &= 2RT/(n_e Fr)\sinh^{-1}\big(i/\big(2i_{0,An}\big)\big) \\ &+ 2RT/(n_e Fr)\sinh^{-1}\big(i/\big(2i_{0,Ca}\big)\big) \end{aligned} \tag{20}$$

$$i_{0,An} = \Upsilon_{An}(P^{H_2}/P_0)(P^{H_2O}/P_0)exp\big(-E_{Act,An}/(RT)\big) \tag{21}$$

$$i_{0.Ca} = \Upsilon_{Ca}(P^{O_2}/P_0)^{0.25}exp\big(-E_{Act,Ca}/(RT)\big) \tag{22}$$

Υ_i are exchange current density pre-exponential factor and $E_{Act,i}$ are activation energies [46]. Partial pressures of gasses are related to their molar concentrations in $An4$ that were already calculated in section 3.1. Then for ohmic and concentration polarization following equations can be written [47,48].

$$v_{Ohm} = \sum ir = \sum i\delta\underline{A} \times exp\big(\underline{B}/T\big) \tag{23}$$

$$v_{Conc} = (RT/(n_e Fr))(1 - i/i_l) \tag{24}$$

Constants to calculate ohmic polarization are presented in Table 3.

Table 3: Constants to calculate ohmic polarization [47,48]

	$\underline{A}(\Omega.cm)$	$\underline{B}(K)$	$\delta(cm)$
Anode	0.00298	1392	0.01
Cathode	0.00814	-600	0.19
Electrolyte	0.00294	-10350	0.004
Internal connections	0.1256	-4690	0.0085

Now to calculate cell voltage, at first based on equations (20) - (22) activation polarization (v_{Act}), based on equation (23), ohmic polarization (v_{Ohm}), and based on equation (24), concentration polarization (v_{Conc}) should be calculated. Then these values based on equation (19) are extracted from the reversible voltage (v_{rev}) that can be calculated based on equation (18) to calculate cell voltage (v).

3.3. IRSOFC Temperature

IRSOFC temperature can be calculated based on a trial and error method. The energy balance is based on the idea that the heat generation inside IRSOFC should be equal to the energy increment of gasses pass through it. Thus, thermal energy generation/consumption due to three main equations inside IRSOFC (Eqs. (1)-(3)) and due to irreversibilities of polarizations should be calculated and compared to the required energy to increase the temperature of reactants and products to the cell temperature. Based on this idea, the temperature of the IRSOFC is calculated [49]. The heat production due to irreversibilities and also electrochemical reaction inside IRSOFC are as follows:

$$Q_{rxn} = i_{cell} A_{cell} (v_{Act} + v_{Ohm} + v_{Conc}) + T_{cell} \Delta S \quad (25)$$

$$\Delta S = \left(S_0^{H_2O} - S_0^{H_2} - (1/2)\, S_0^{O_2}\right) - R \ln(P^{H_2} (P^{O_2})^{0.5} / P^{H_2O}) \quad (26)$$

The required heat for reforming and shifting processes can also be calculated as:

$$Q_r = a(H^{CO} + 3H^{H_2} - H^{H_2O} - H^{CH_4}) \quad (27)$$

$$Q_s = b(H^{CO_2} + H^{H_2} - H^{H_2O} - H^{CO}) \quad (28)$$

The produced heat (Eq. (25)) is used to provide required heat for the reforming and shifting reactions (Eqs. (27) and (28)), and also, to heat the gas streams, that can be calculated as:

$$\begin{aligned} Q_{heat\ up} = &\left(\dot{n}_{An,re} \int_{T_{An}}^{T_{cell}} Cp\ dT\right)_{re} + \left(\dot{n}_{An,pr} \int_{T_{An}}^{T_{cell}} Cp\ dT\right)_{pr} \\ &+ \left(\dot{n}_{Ca,re} \int_{T_{Ca}}^{T_{cell}} Cp\ dT\right)_{re} + \left(\dot{n}_{Ca,pr} \int_{T_{Ca}}^{T_{cell}} Cp\ dT\right)_{pr} \end{aligned} \quad (29)$$

Now, the remaining thermal energy of the reactions are compared to the required energy for the heat up to calculate the cell temperature through a trial and error procedure. The heat transfer with the surrounding is also ignored.

$$Error = \left(Q_{heat\ up} - (Q_{rxn} - Q_r - Q_s)\right) / (Q_{rxn} - Q_r - Q_s) < 1\% \quad (30)$$

The procedure of the temperature calculation is shown in Figure 4.

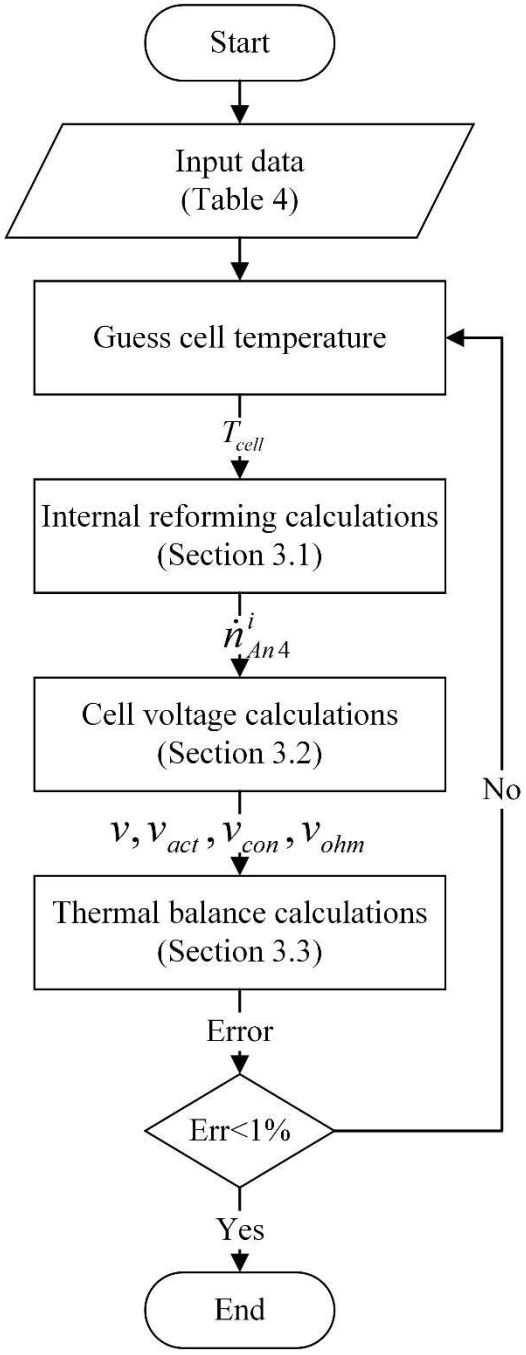

Figure 4: Flowchart of trial and error procedure for IRSOFC temperature calculation

3.4. IRSOFC Results and Validation

The IRSOFC is modeled in MATLAB® with the equations presented in the previous section. In order to validate it, the results of the modeling are compared with Pirkandi et al. [49] ones (Figure 5 - Figure 9), considering the same input data, which is shown in Table 4.

Table 4: IRSOFC input data for validation

U_f	0.85
U_{ox}	0.25
Re	60 %

P	1 bar
A_{cell}	0.10362 m^2
i_l	9000 A/m^2
Number of cells	8792

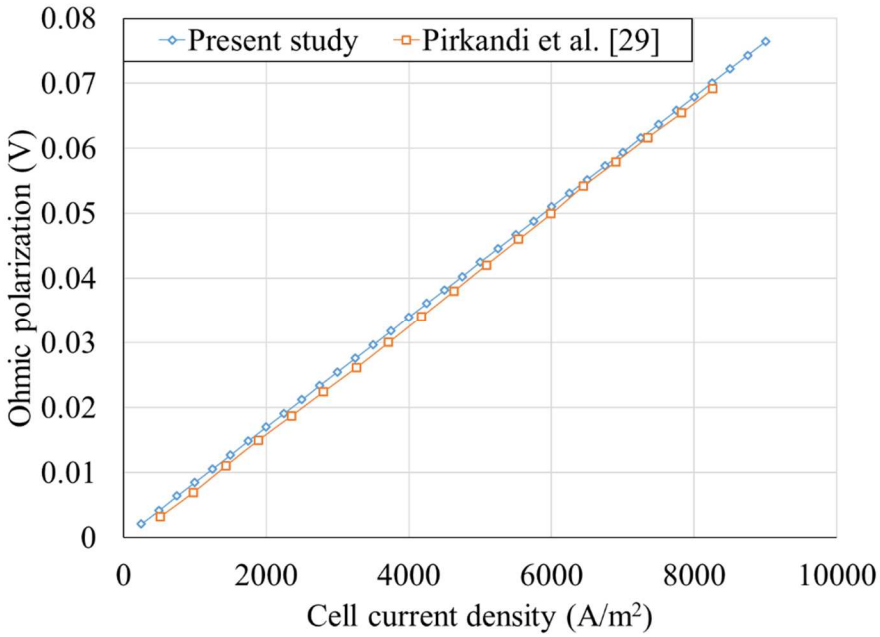

Figure 5: Validation of ohmic polarization

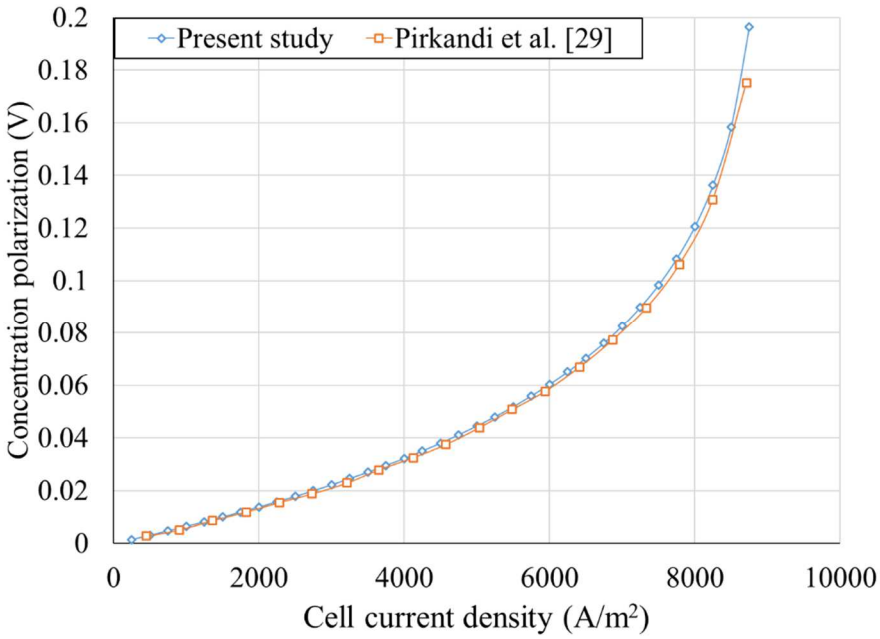

Figure 6: Validation of concentration polarization

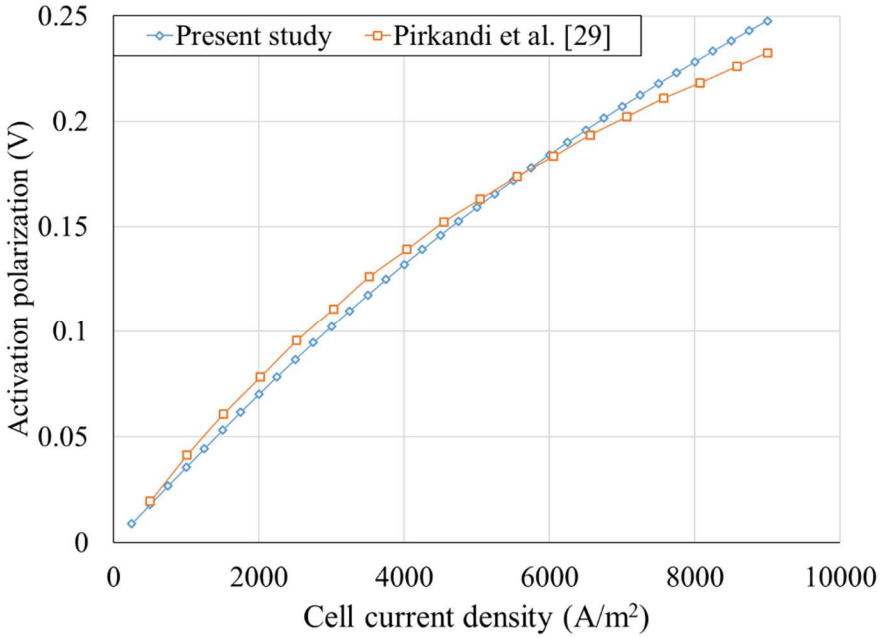

Figure 7: Validation of activation polarization

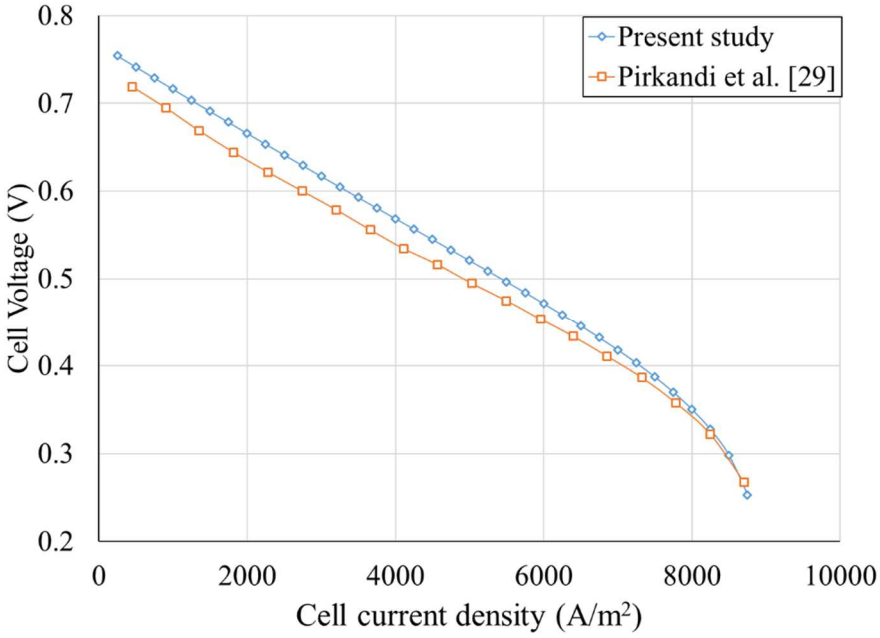

Figure 8: Validation of cell voltage

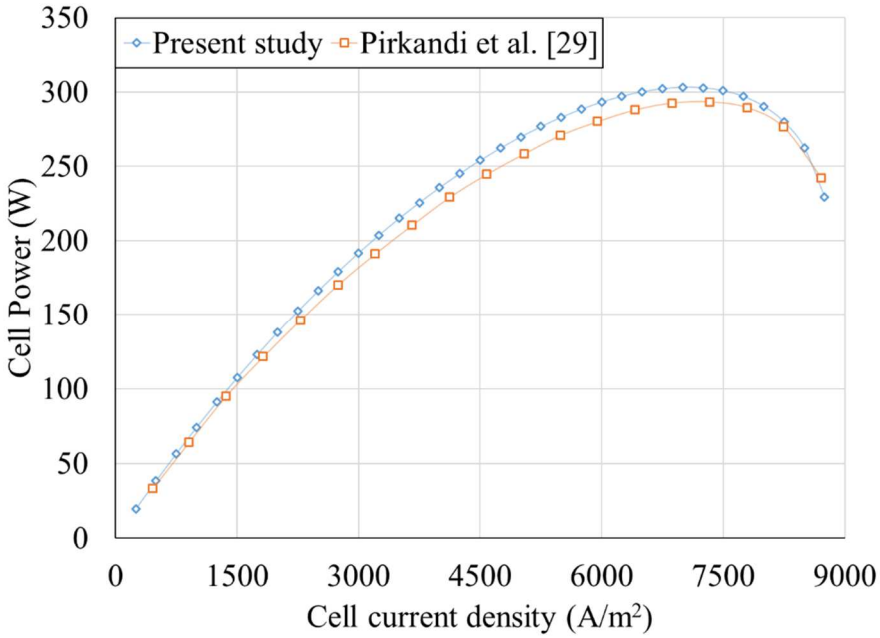

Figure 9: Validation of cell power

As can be seen in Figure 5 - Figure 9, there is a good agreement between the present study and Pirkandi et al. [49] results that shows the IRSOFC model is valid. The effect of the current density on the power and voltage is also shown. By increasing the current density, the voltage of the cell is continuously decreasing. Also, this increment increases the power by a point, and after that (around 7500 A/m^2), the power decreases. It is important to choose an appropriate working current density for the system to satisfy the requirements.

4. FPSE-PMLSM Analysis

There are three types of Stirling engines: alpha, beta, and gamma. For the present study, due to the higher power density of the beta-type compared to alpha and gamma-type Stirling engines, the beta-type Stirling engine is chosen [50]. The schematic of the FPSE combined with the PMLSM is shown in Figure 10.

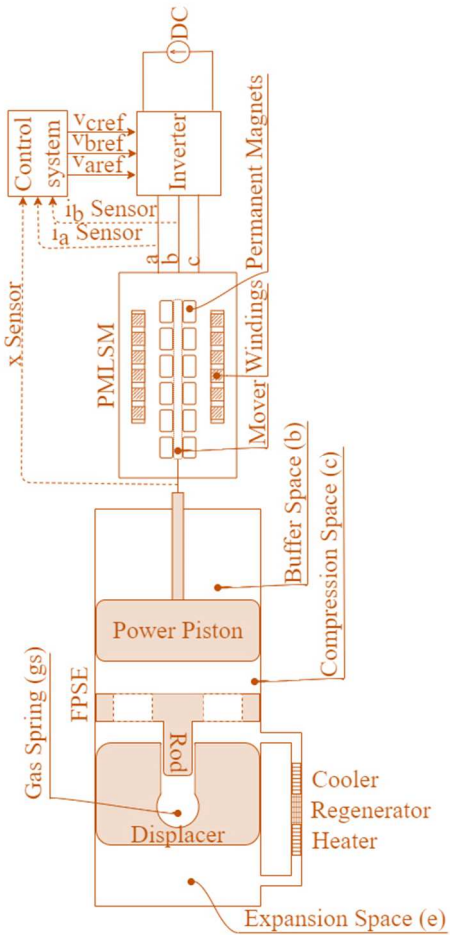

Figure 10: FPSE-PMLSM schematic [40]

The FPSE system is a beta type Sunpower RE-1000 engine, and the PMLSM is a three-phase one. The FPSE converts thermal energy into linear movement. This produced linear movement in the power piston is transferring to the PMLSM mover through a rod. In PMLSM, the linear movement of the rod is converting to electrical power. A control system is also used beside an inverter to control the combined system.

Based on the main spaces of the FPSE dynamic equations for the combined system around power piston (p subscript) and displacer piston (D subscript) can be written as [40]:

$$\left(m_p + m_m\right)\ddot{x}_p = A_p(P_c - P_b) + F_{em} - B_v\dot{x}_p \tag{31}$$

$$m_D\ddot{x}_D = A_D P_e - (A_D - A_{rod})P_c - A_{rod}\left(P_{gs}\right) = A_D(P_e - P_c) + A_{rod}\left(P_c - P_{gs}\right) \tag{32}$$

In these equations, at first, pressures and electromagnetic force should be calculated to be able to calculate $\ddot{x}_i$, $\dot{x}_i$, and finally x_i. Pressures of buffer space (P_b) and displacer gas spring space (P_{gs}) can be calculated based on the adiabatic assumption [40]:

$$P_i = P^{mean}\left(V_i^{mean}/V_i^{\text{instantaneous}}\right)^{\lambda} \quad i: b, gs \tag{33}$$

Compression pressure at each moment can be calculated as [40]:

$$P_c = MR\left(\frac{V_c}{T_c} + \frac{V_e}{T_e} + \frac{V_h}{T_h} + \frac{V_k}{T_k} + \frac{V_{R1}}{T_{R1}} + \frac{V_{R2}}{T_{R2}}\right)^{-1} \tag{34}$$

In equation (34) V_i and T_i are instantaneous values. M is total mass, which is constant. As can be seen, to have a more precise model of the regenerator, it is divided into two parts ($R1, R2$). Other pressures can be calculated based on P_c and pressure drops in the heater, cooler, and regenerator. Details of the pressure drops calculations have been already discussed by Majidniya et al. [40], which are based on the following nonlinear equation:

$$\Delta P = \frac{1}{2}\rho\left(\frac{C_f l}{d_{hydraulic}}\right)u|u| \tag{35}$$

Also, T_i of equation (34) can be calculated based on the energy equation in each space:

$$\dot{Q}_{in} + (\dot{m}CpT)_{in} - (\dot{m}CpT)_{out} - \dot{W}_{out} = Cv\frac{d}{dt}(mT) \tag{36}$$

For spaces with constant volumes (heater, cooler, and regenerator), there is no work ($\dot{W}_{out} = 0$) and for expansion and compression spaces, it is assumed that there is no heat transfer with the environment ($\dot{Q}_{in} = 0$). Here two key parameters are $\dot{m}_{in\,\&\,out}$ and $T_{in\,\&\,out}$. For temperatures, it is assumed that when the mass flows from space i to space j, the temperature in the boundary is equal to T_i and vice versa. To calculate the mass flow rates in boundaries, at first, the mass variation at each space is calculated. Then, based on these mass variations, the mass flow rate at each boundary can be calculated. For example, the mass flow rate from cooler to compression space is equal to mass variation in compression space. It means that the summation of mass variations before/after each boundary is equal to the mass flow rate through that boundary. For example, the summation of mass variations in cooler and compression space is the mass flow rate from the first part of the regenerator ($R1$) to cooler. In order to calculate heat flow in heater, cooler, and regenerator, the following equation can be used:

$$\dot{Q}_i = h_i A_i^{wetted}\left(T_i^{wall} - T_i\right) \qquad i: h, k, R1, R2 \tag{37}$$

After solving equation (36), instantaneous gas temperatures in each space can be calculated. A more detailed thermodynamic model of the FPSE was presented in [41]. Furthermore, PMLSM equations in $d-q$ frame to model the combined system are as [40]:

$$v_d = L_d\frac{di_d}{dt} + ri_d - \frac{\pi}{\tau}\dot{x}L_q i_q \tag{38}$$

$$v_q = L_q\frac{di_q}{dt} + ri_q + \frac{\pi}{\tau}\dot{x}\left(L_d i_d + \sqrt{3/2}\,\psi_f\right) \tag{39}$$

$$F_{em} = \frac{\pi}{\tau}\left(\sqrt{3/2}\,\psi_f i_q + \left(L_d - L_q\right)i_d i_q\right) \tag{40}$$

$$Power_{em} = F_{em}\dot{x}_p \tag{41}$$

$$Power_{el} = v_q i_q + v_d i_d \tag{42}$$

The input parameters of PMLSM are presented in Table 5.

Table 5: Input parameters of PMLSM

r	0.1 (Ω)	L_q	3.01 (mH)
L_d	1.77 (mH)	ψ_f	0.0513 (Wb)

To control the combined system, two PR controllers (for i_q and $\dot{x}_p$) and one PI controller (for i_d) are used. The model of the FPSE-PMLSM system is developed in MATLAB Simulink®.

4.1. FPSE-PMLSM Results and Validation

Before coupling FPSE with PMLSM, its equations based on Schreiber [51] input data (shown in Table 6) are solved, and the results are presented in Table *7*. These input data and experimental results have also been used by the recently published articles [40,41] to validate the FPSE model.

Table 6: FPSE input data for validation

T_h^{wall}	814.3 K
T_k^{wall}	322.8 K
T_{R1}^{wall}	418.4 K
T_{R2}^{wall}	662.7 K
P^{mean}	71 bars
$Porosity$	75.9 %
m_D	0.426 kg
m_p	6.2 kg
d_p	5.718 cm
d_D	5.67 cm
d_{rod}	1.663 cm
d_h	0.2362 cm
d_w	0.00889 cm
L_k	7.92 cm
L_h	18.34 cm
L_R	6.44 cm
A_h	1.4898 cm^2
A_k	2.6163 cm^2
$A_{R1,R2}$	8.745 cm^2
C_c	1.83 cm
C_e	1.861 cm
V_b^{mean}	2615 cm^3
V_{gs}^{mean}	37.97 cm^3
$V_{R1,R2}$	28.185 cm^3
A_k^{wetted}	115.2 cm^2

Table 7: Validation of FPSE thermodynamic model

	Exp. [51]	Theoretical	Error (%)

Power (W)	1000	1003.9	0.39
Frequency (Hz)	30.2	28.57	5.4
Phase Shift (°)	47.6	32.94	30.8
$Stroke_p$ (cm)	2.32	2.746	18.4
$Stroke_d$ (cm)	2.55	2.379	6.7
Efficiency (%)	27.4	30.02	9.56

As can be seen, the FPSE model is valid. After that, the thermodynamic-electric coupled model of FPSE-PMLSM is solved, and the combined system is controlled. The results of the combined model are presented in Figure 11 - Figure 14.

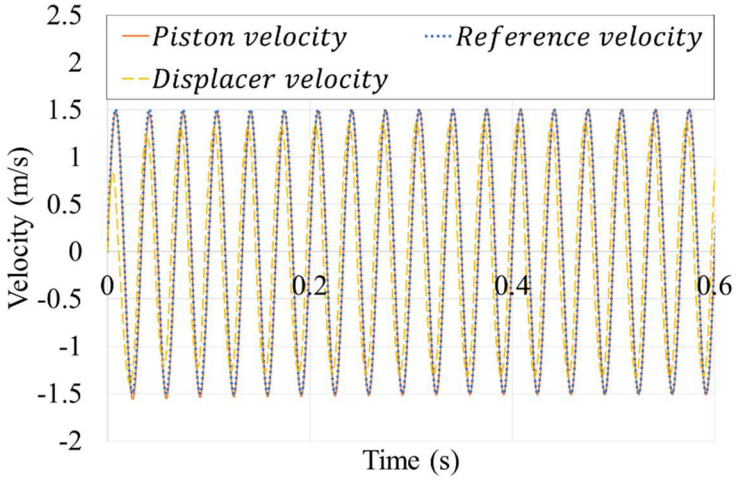

Figure 11: Velocity variations

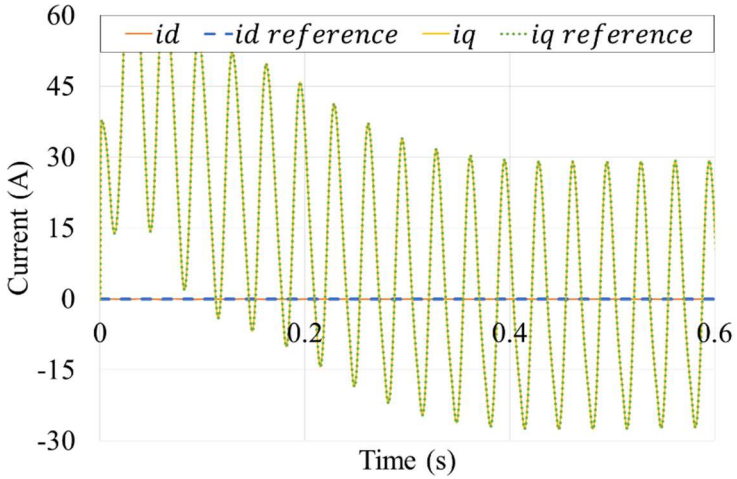

Figure 12: Current variations

As shown in Figure 11 and Figure 12, the system based on one PI and two PR controllers is well controlled. All the parameters are precisely following their reference values.

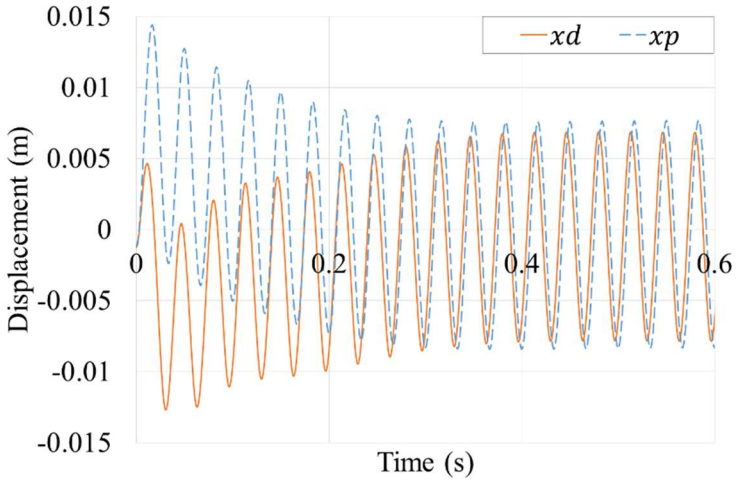

Figure 13: Displacement variations

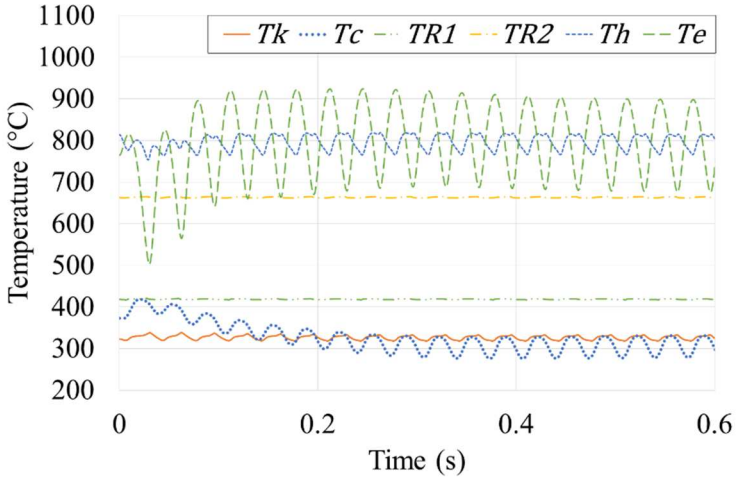

Figure 14: Temperature variations

In Figure 13 and Figure 14, the variations of thermic and dynamic properties of the system are shown. As can be seen, the system is stabilized after around 0.4 (s). The variations of temperatures in Figure 14 in steady-state are always around a specific value. The periodic behavior of the system causes the periodic fluctuations of the temperatures. Regenerators' temperatures are almost constant, and the expansion temperature has the maximum range of variations.

5. DEACH

The Schematic of the DEACH is shown in Figure 15. The refrigerant and the absorbents are water and lithium bromide, respectively. The following assumptions are made to model the DEACH system:

- The system operates at steady-state
- The refrigerant that leaves the condenser is saturated liquid
- The refrigerant that leaves the evaporator is saturated vapor
- The pressure drop inside tubes is neglected
- The pump work is neglected
- The heat transfer with outside happens only in the evaporator, condenser, absorber, and high-pressure generator
- The processes in expansion valves are enthalpy constant

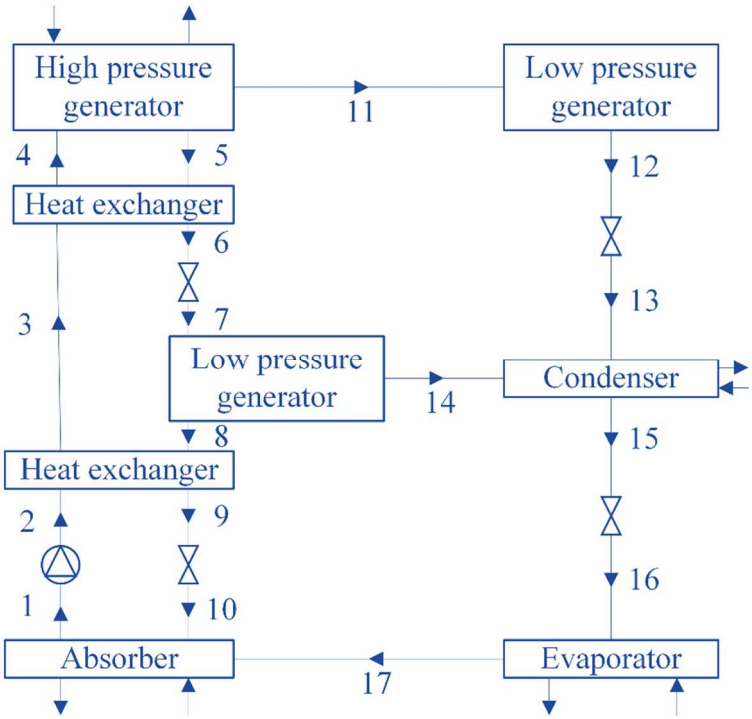

Figure 15: Schematic of DEACH

Components of the DEACH are in three pressure levels and five temperature levels. For each component, the laws of conservation of mass and energy are applied by calculating each flow's properties. For a lithium bromide solution, the enthalpy can be calculated as [52]:

$$H = 2.326\{\underline{A}_1 + \underline{A}_2(1.8T + 32) + \underline{A}_3(1.8T + 32)^2\} \tag{43}$$

A_i can be calculated as [52]:

$$\underline{A}_i = \underline{a}_0 + \underline{a}_1 Xm + \underline{a}_2 Xm^2 + \underline{a}_3 Xm^3 + \underline{a}_4 Xm^4 \tag{44}$$

Table 8: Constants to calculate the enthalpy of lithium bromide solution [52]

	$\underline{A}_1$	$\underline{A}_2$	$\underline{A}_3$
$\underline{a}_0$	-1015.07	4.68108	-4.9107×10^{-3}
$\underline{a}_1$	79.5387	-3.037766×10^{-1}	3.83184×10^{-4}
$\underline{a}_2$	-2.358016	8.44845×10^{-3}	-1.078963×10^{-5}
$\underline{a}_3$	0.03031583	-1.047721×10^{-4}	1.3152×10^{-7}
$\underline{a}_4$	-1.400261×10^{-4}	4.80097×10^{-7}	-5.897×10^{-4}

Xm is the mass concentration of lithium bromide in the solution. T is the solution temperature, which can be calculated as [52]:

$$T = T_{\text{Dew Point}} \sum_{n=0}^{3} \underline{A}_n Xm^n + \sum_{n=0}^{3} \underline{B}_n Xm^n \tag{45}$$

A_n and B_n are constants that are shown in Table 9.

Table 9: Constants of solution temperature formula [52]

n	$\underline{A}_n$	$\underline{B}_n$
0	-2.00755	124.934
1	0.16976	-7.7165
2	-3.13336×10^{-3}	0.152286
3	1.97668×10^{-5}	-7.9509×10^{-4}

To validate the DEACH, it is run based on Gebreslassie et al. [53] conditions shown in Table 10, and the results are presented in Table 11.

Table 10: Five-level temperatures of DEACH

Evaporator	280.15 K
Absorber	305.15 K
Low-pressure generator	340.95 K
High-pressure generator	381.05 K
Condenser	305.35 K

Table 11: DEACH validation

Flow number	Temperature (K)	
	Present study	Gebreslassie et al. [53]
1	305.15	305.15
2	305.15	305.15
3	337.055	337.95
4	378.39	379.15
5	381.05	382.95
6	337.055	338.15
7	337.055	338.15
8	340.95	343.75
9	305.15	305.35
10	305.15	305.35
11	381.05	381.05
12	343.426	343.95
13	305.35	305.35
14	340.95	340.95
15	305.35	305.35

16	280.15	280.15
17	280.15	280.15
Flow number	Pressure (kPa)	
	Present study	Present study
1	1.0021	1.0021
2	31.575	31.575
3	31.575	31.575
4	31.575	31.575
5	31.575	31.575
6	31.575	31.575
7	4.8133	4.8133
8	4.8133	4.8133
9	4.8133	4.8133
10	1.0021	1.0021
11	31.575	31.575
12	31.575	31.575
13	4.8133	4.8133
14	4.8133	4.8133
15	4.8133	4.8133
16	1.0021	1.0021
17	1.0021	1.0021
Flow number	Concentration (%)	
	Present study	Present study
1	53.95	53.95
2	53.95	53.95
3	53.95	53.95
4	53.95	53.95
5	55.92	55.92
6	55.92	55.92
7	55.92	55.92
8	57.65	57.65
9	57.65	57.65

10	57.65	57.65
11	-	-
12	-	-
13	-	-
14	-	-
15	-	-
16	-	-
17	-	-

Flow number	Enthalpy (kJ/kg)	
	Present study	Gebreslassie et al. [53]
1	73.583	73.1
2	73.583	73.2
3	140.46	142.3
4	227.43	230.9
5	235.96	241.4
6	145.82	148.3
7	145.82	148.3
8	159.61	167
9	88.152	91.1
10	88.152	91.1
11	2700.1	2700
12	294.17	296.4
13	294.17	296.4
14	2627.1	2627.1
15	134.94	134.9
16	134.94	134.9
17	2513.7	2513.7

Also, the *COP* of the Gebreslassie et al. [53] model was 1.655, while the present study has a *COP* of 1.6012. As can be seen, the present model of the DEACH is valid and presents almost the same results as Gebreslassie et al. [53] study. The model of the DEACH is developed in MATLAB®.

6. Combined system analysis

After modeling, presenting the results, and validating each system, they are coupled based on Figure 1. At first, the high-quality output heat of the IRSOFC is used for running the FPSE-

PMLSM system. Then to increase the temperature and burn the left output gas of the IRSOFC, it passes through a combustion chamber. After that, the reheated gas is used for preheating the input air and fuel of the IRSOFC. Then, it provides the required heat of the DEACH. The final low-quality heat is used to produce the required hot water.

The input parameters of the combined system are presented in Table 12. For a better understanding of FPSE input data, its schematic is shown in Figure 16, that all the spaces and parameters can be located.

Table 12: Combined system input parameters

FPSE input parameters	
T_h^{wall}	883.7 K
T_k^{wall}	322.8 K
T_{R1}^{wall}	429.3 K
T_{R2}^{wall}	707.8 K
P^{mean}	71 bars
$Porosity$	75.9 %
m_D	0.426 kg
m_p	6.2 kg
d_p	5.718 cm
d_D	5.67 cm
d_{rod}	1.663 cm
d_h	0.2362 cm
d_w	0.00889 cm
L_k	7.92 cm
L_h	18.34 cm
L_R	6.44 cm
A_h	1.4898 cm^2
A_k	2.6163 cm^2
$A_{R1,R2}$	8.745 cm^2
C_c	1.83 cm
C_e	1.861 cm
V_b^{mean}	2615 cm^3
V_{gs}^{mean}	37.97 cm^3
$V_{R1,R2}$	28.185 cm^3
A_k^{wetted}	115.2 cm^2
IRSOFC input parameters	

U_f	0.85
U_{ox}	0.25
Re	60 %
P	1 bar
A_{cell}	0.0834 m^2
i_{cell}	2000 A/m^2
i_l	9000 A/m^2
Number of cells	26
PMLSM input parameters	
ψ_f	0.0513 Wb
B_v	10
m_m	0.824 kg
r	0.1 Ω
L_d	1.77 mH
L_q	3.01 mH

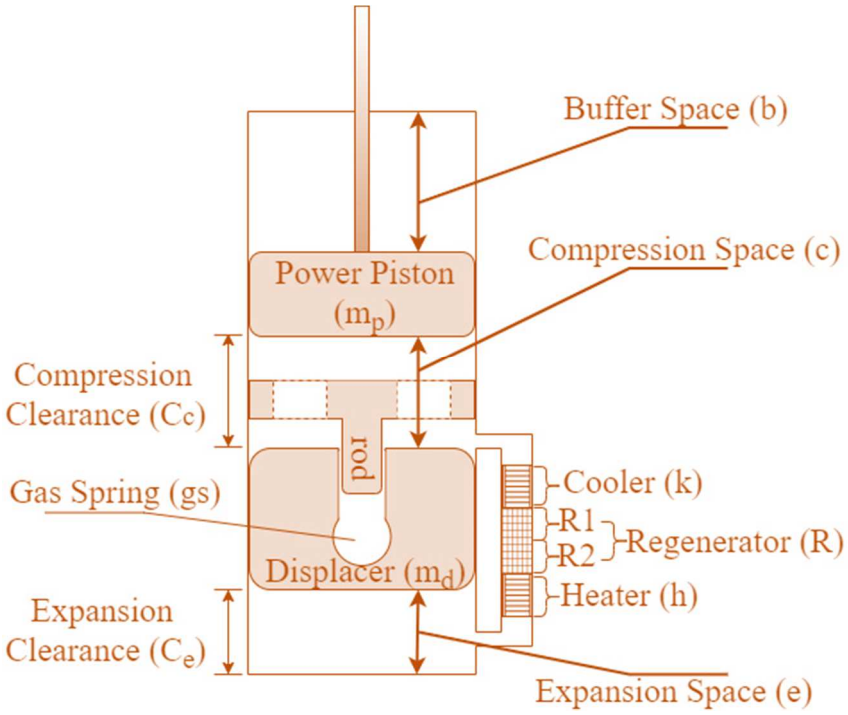

Figure 16: FPSE schematic

Based on these input data and DEACH temperature levels of Table 10, the systems are combined. For IRSOFC, based on input data of Table 12, the calculated operating temperature is 1000 K. The output of each system in the combined mode is shown in Table 13.

Table 13: System output

IRSOFC	1981 W
FPSE-PMLSM	279.4 W
DEACH	1366.6 W
Hot water	0.27 kg/s
Input heat	6165.4 W

As can be seen, IRSOFC and FPSE-PMLSM electricity production, DEACH cooling production, and produced hot water flow rate are shown in Table 13. The equation which is used to calculate IRSOFC power production is as follows:

$$Power_{IRSOFC} = (Number\ of\ Cells) \times i_{cell} A_{cell} v \tag{46}$$

FPSE-PMLSM power production is also calculated based on equation (42). The hot water thermal flowrate also can be calculated as:

$$\dot{Q}_{Hotwater} = \dot{m}_{water} Cp_{water} \times (T_{water\ hot} - T_{water\ cold}) \tag{47}$$

It is assumed that the hot water temperature ($T_{water\ hot}$) is 333.15 K that should be achieved from the cold water ($T_{water\ cold}$) at 298.15 K. Also, the input thermal energy is calculate based on the input fuel (CH_4) flow rate to IRSOFC and its LHV (Lower Heating Value).

$$\dot{Q}_{Input} = \dot{m}_{CH_4} LHV \tag{48}$$

Now, the efficiency of this combined system can be calculated. To calculate efficiency, two methods can be defined based on the following equation:

$$\eta = \frac{Power_{IRSOFC} + Power_{FPSE-PMLSM} + \dot{Q}_{DEACH} + \dot{Q}_{Hotwater}}{\dot{Q}_{Input}} \tag{49}$$

In this equation, powers are output electrical powers, and $\dot{Q}_{Hotwater}$ is the amount of heat that was recovered by heating the water. $\dot{Q}_{DEACH}$ can be defined as the heat that is used in DEACH or the cooling that is produced by it. If it is assumed that $\dot{Q}_{DEACH}$ is the consumed heat in DEACH, the whole combined system efficiency is equal to 63.82 %, but if $\dot{Q}_{DEACH}$ is the cooling production, the efficiency of the combined system is equal to 72.14%. Comparing this system with a standalone IRSOFC, which has an efficiency of 32.13%, shows that the total efficiency of the system based on the first and the second method of efficiency calculation is increased by 31.7% and 40%, respectively. Also, based on the electrical efficiency of the system, according to Table 13, the efficiency of the combined system is 36.66%, which shows around 14.1% increment compared to the standalone IRSOFC. All these results show a significant improvement of the IRSOFC performance when it works in a combined system with an FPSE-PMLSM, a DEACH, and a heat exchanger to produce hot water.

7. Conclusion

In the present study, a new power production system, which was an FPSE-PMLSM one, was proposed as a heat recovery option for an IRSOFC. To recover the final residual heat of the IRSOFC, a DEACH, and a heat exchanger to produce cooling and hot water, respectively, were also added to the system. At first, the IRSOFC was modeled and validated using polarization and power curves at different current densities. Then, a nonlinear thermodynamic model of the FPSE was presented and validated at 1 kW of power production. After that, the PMLSM was modeled and coupled with the FPSE, and the combined system was controlled using two PR

and one PI controller. After presenting each system's results in different sections, they were combined, and the results of the combined system were presented. The goal of this combined system was to produce electrical power (by IRSOFC and FPSE-PMLSM), cooling (by DEACH), and hot water (by heat exchanger). Two methods were applied to calculate the system efficiency. In the first method, the consumed heat of DEACH was assumed as the useful energy, and in the second method, the cooling production of the DEACH was used to calculate the efficiency.

The results showed that the combined system produced 1981 W power by IRSOFC and 279.4 W by FPSE-PMLSM system. Thus, the total produced electrical power was 2260.4 W, which was around 14% more than the standalone IRSOFC system. This meant around a 4.5% increment in electrical efficiency. The combined system also produced around 1367 W of cooling by the DEACH, and 0.27 kg/s of hot water at 333.15 K by the heat exchanger. Based on these data and two different methods, the efficiency of the system was calculated. At first, it was assumed that all the productions (electrical power, cooling, required heat for hot water production) were the system's output that was used for efficiency calculation. In this case, the system efficiency was around 72%, which was 40% higher than the standalone IRSOFC with around 32% of efficiency. Then, only the recovered heat (by the heat exchanger and DEACH) was used besides the produced electrical power (by IRSOFC and FPSE-PMLSM) for efficiency calculation. In this case, the total efficiency of the system was around 63%, which was around 32% higher than the standalone IRSOFC. In any case, these results showed the significant effect of adding the FPSE and other auxiliary heat recovery systems to the IRSOFC system.

References

[1] E. Theo, A novel SOFC tri-generation system for building applications, Springer, 2015.

[2] T.H. Kwan, F. Katsushi, Y. Shen, S. Yin, Y. Zhang, K. Kase, Q. Yao, Comprehensive review of integrating fuel cells to other energy systems for enhanced performance and enabling polygeneration, Renew. Sustain. Energy Rev. 128 (2020) 109897. https://doi.org/10.1016/j.rser.2020.109897.

[3] S.M.J. Zaidi, M.A. Rauf, Fuel cell fundamentals, John Wiley & Sons, 2009. https://doi.org/10.1007/978-0-387-73532-0_1.

[4] S.C. Singhal, Solid Oxide Fuels Cells: Facts and Figures, Springer, 2013. http://www.scopus.com/inward/record.url?eid=2-s2.0-84883167213&partnerID=tZOtx3y1.

[5] A.C. Ferreira, J. Silva, S. Teixeira, J.C. Teixeira, S.A. Nebra, Assessment of the Stirling engine performance comparing two renewable energy sources: Solar energy and biomass, Renew. Energy. 154 (2020) 581–597. https://doi.org/10.1016/j.renene.2020.03.020.

[6] M.A. Al-Nimr, W.A. Al-Ammari, A novel hybrid and interactive solar system consists of Stirling engine/vacuum evaporator/thermoelectric cooler for electricity generation and water distillation, Renew. Energy. 153 (2020) 1053–1066. https://doi.org/10.1016/j.renene.2020.02.072.

[7] Ł. Bartela, J. Kotowicz, L. Remiorz, A. Skorek-Osikowska, K. Dubiel, Assessment of the economic appropriateness of the use of Stirling engine as additional part of a cogeneration system based on biomass gasification, Renew. Energy. 112 (2017) 425–443. https://doi.org/10.1016/j.renene.2017.05.028.

[8] M. Marion, H. Louahlia, H. Gualous, Performances of a CHP Stirling system fuelled with glycerol, Renew. Energy. 86 (2016) 182–191. https://doi.org/10.1016/j.renene.2015.08.012.

[9] M. Rokni, Biomass gasification integrated with a solid oxide fuel cell and Stirling engine, Energy. 77 (2014) 6–18. https://doi.org/10.1016/j.energy.2014.01.078.

[10] D. Sánchez, R. Chacartegui, M. Torres, T. Sánchez, Stirling based fuel cell hybrid systems: An alternative for molten carbonate fuel cells, J. Power Sources. 192 (2009) 84–93. https://doi.org/10.1016/j.jpowsour.2008.12.061.

[11] X.J. Luo, K.F. Fong, Investigation on part-load performances of combined cooling and power system primed by solid oxide fuel cell with different bottoming cycles, J. Power Sources. 429 (2019) 127–148. https://doi.org/10.1016/j.jpowsour.2019.04.095.

[12] S. Obara, I. Tanno, S. Kito, A. Hoshi, S. Sasaki, Exergy analysis of the woody biomass Stirling engine and PEM-FC combined system with exhaust heat reforming, Int. J. Hydrogen Energy. 33 (2008) 2289–2299. https://doi.org/10.1016/j.ijhydene.2008.02.035.

[13] M. Rokni, Thermodynamic analysis of SOFC (solid oxide fuel cell)-Stirling hybrid plants using alternative fuels, Energy. 61 (2013) 87–97. https://doi.org/10.1016/j.energy.2013.06.001.

[14] M. Rokni, Thermodynamic and thermoeconomic analysis of a system with biomass gasification, solid oxide fuel cell (SOFC) and Stirling engine, Energy. 76 (2014) 19–31. https://doi.org/10.1016/j.energy.2014.01.106.

[15] M. Rokni, Thermodynamic analyses of municipal solid waste gasification plant integrated with solid oxide fuel cell and Stirling hybrid system, Int. J. Hydrogen Energy. 40 (2015) 7855–7869. https://doi.org/10.1016/j.ijhydene.2014.11.046.

[16] J.M. Muñoz De Escalona, D. Sánchez, R. Chacartegui, T. Sánchez, Performance analysis of hybrid systems incorporating high temperature fuel cells and closed cycle heat engines at part-load operation, Int. J. Hydrogen Energy. 38 (2013) 570–578. https://doi.org/10.1016/j.ijhydene.2012.07.082.

[17] L. Chen, H. Zhang, S. Gao, H. Yan, Performance optimum analysis of an irreversible molten carbonate fuel cell-Stirling heat engine hybrid system, Energy. 64 (2014) 923–930. https://doi.org/10.1016/j.energy.2013.10.052.

[18] M. Mehrpooya, S. Sayyad, M.J. Zonouz, Energy, exergy and sensitivity analyses of a hybrid combined cooling, heating and power (CCHP) plant with molten carbonate fuel cell (MCFC) and Stirling engine, J. Clean. Prod. 148 (2017) 283–294. https://doi.org/10.1016/j.jclepro.2017.01.157.

[19] J. Hosseinpour, M. Sadeghi, A. Chitsaz, F. Ranjbar, M.A. Rosen, Exergy assessment and optimization of a cogeneration system based on a solid oxide fuel cell integrated with a Stirling engine, Energy Convers. Manag. 143 (2017) 448–458. https://doi.org/10.1016/j.enconman.2017.04.021.

[20] H. Ansarinasab, M. Mehrpooya, Investigation of a combined molten carbonate fuel cell, gas turbine and Stirling engine combined cooling heating and power (CCHP) process by exergy cost sensitivity analysis, Energy Convers. Manag. 165 (2018) 291–303. https://doi.org/10.1016/j.enconman.2018.03.067.

[21] A. Habibollahzade, E. Gholamian, E. Houshfar, A. Behzadi, Multi-objective optimization of biomass-based solid oxide fuel cell integrated with Stirling engine and electrolyzer, Energy Convers. Manag. 171 (2018) 1116–1133. https://doi.org/10.1016/j.enconman.2018.06.061.

[22] M. Marefati, M. Mehrpooya, S.A. Mousavi, Introducing an integrated SOFC, linear Fresnel solar field, Stirling engine and steam turbine combined cooling, heating and power process, Int. J. Hydrogen Energy. 44 (2019) 30256–30279. https://doi.org/10.1016/j.ijhydene.2019.09.074.

[23] A. Salehi, S.M. Mousavi, A. Fasihfar, M. Ravanbakhsh, Energy, exergy, and environmental (3E) assessments of an integrated molten carbonate fuel cell (MCFC), Stirling engine and organic Rankine cycle (ORC) cogeneration system fed by a biomass-fueled gasifier, Int. J. Hydrogen Energy. 44 (2019) 31488–31505. https://doi.org/10.1016/j.ijhydene.2019.10.038.

[24] I. Moradpoor, M. Ebrahimi, Thermo-environ analyses of a novel trigeneration cycle based on clean technologies of molten carbonate fuel cell, stirling engine and Kalina cycle, Energy. 185 (2019) 1005–1016. https://doi.org/10.1016/j.energy.2019.07.112.

[25] M. Moradi, B. Ghorbani, R. Shirmohammadi, M. Mehrpooya, M.H. Hamedi, Developing of an integrated hybrid power generation system combined with a multi-effect desalination unit, Sustain. Energy Technol. Assessments. 32 (2019) 71–82. https://doi.org/10.1016/j.seta.2019.02.002.

[26] L. Mantelli, M. De Campo, M.L. Ferrari, L. Magistri, Fuel flexibility for a turbocharged SOFC system, Energy Procedia. 158 (2019) 1974–1979. https://doi.org/10.1016/j.egypro.2019.01.454.

[27] M.A. Emadi, N. Chitgar, O.A. Oyewunmi, C.N. Markides, Working-fluid selection and thermoeconomic optimisation of a combined cycle cogeneration dual-loop organic Rankine cycle (ORC) system for solid oxide fuel cell (SOFC) waste-heat recovery, Appl. Energy. 261 (2020) 114384. https://doi.org/10.1016/j.apenergy.2019.114384.

[28] K.H. Lee, R.K. Strand, SOFC cogeneration system for building applications, part 1: Development of SOFC system-level model and the parametric study, Renew. Energy. 34 (2009) 2831–2838. https://doi.org/10.1016/j.renene.2009.04.010.

[29] G.N. Prodromidis, F.A. Coutelieris, Solid Oxide Fuel Cell systems for electricity generation: An optimization prospect, Renew. Energy. 146 (2020) 38–43. https://doi.org/10.1016/j.renene.2019.06.049.

[30] C. Wang, Z. Lü, J. Li, Z. Cao, B. Wei, H. Li, M. Shang, C. Su, Efficient use of waste carton for power generation, tar and fertilizer through direct carbon solid oxide fuel cell, Renew. Energy. 158 (2020) 410–420. https://doi.org/10.1016/j.renene.2020.05.082.

[31] R. Cozzolino, L. Lombardi, L. Tribioli, Use of biogas from biowaste in a solid oxide fuel cell stack: Application to an off-grid power plant, Renew. Energy. 111 (2017) 781–791. https://doi.org/10.1016/j.renene.2017.04.027.

[32] D. Papurello, S. Silvestri, L. Tomasi, I. Belcari, F. Biasioli, M. Santarelli, Natural Gas Trace Compounds Analysis with Innovative Systems: PTR-ToF-MS and FASTGC, Energy Procedia. 101 (2016) 536–541. https://doi.org/10.1016/j.egypro.2016.11.068.

[33] D. Papurello, C. Iafrate, A. Lanzini, M. Santarelli, Trace compounds impact on SOFC performance: Experimental and modelling approach, Appl. Energy. 208 (2017) 637–654.

https://doi.org/10.1016/j.apenergy.2017.09.090.

[34] D. Papurello, S. Silvestri, A. Lanzini, Biogas cleaning: Trace compounds removal with model validation, Sep. Purif. Technol. 210 (2019) 80–92. https://doi.org/10.1016/j.seppur.2018.07.081.

[35] N.F. Harun, D. Tucker, T.A. Adams, Technical challenges in operating an SOFC in fuel flexible gas turbine hybrid systems: Coupling effects of cathode air mass flow, Appl. Energy. 190 (2017) 852–867. https://doi.org/10.1016/j.apenergy.2016.12.160.

[36] J. Subramanian, G. Heiskell, F. Mahmudzadeh, P. Famouri, Study of radial and axial magnets for linear alternator - Free piston engine system, in: 2017 North Am. Power Symp. NAPS 2017, IEEE, 2017: pp. 1–6. https://doi.org/10.1109/NAPS.2017.8107293.

[37] R. Redlich, A summary of twenty years experience with linear motors and alternators, Sunpower Inc. (1995) 1–9.

[38] C.K. Alexander, M.N.O. Sadiku, e-Text Fundamentals of Electric Circuits, McGraw-Hill Higher Education, 2001. https://books.google.fr/books?id=SBdigDfQB5cC.

[39] T.T. Dang, M. Ruellan, L. Prévond, H. Ben Ahmed, B. Multon, Sizing Optimization of Tubular Linear Induction Generator and Its Possible Application in High Acceleration Free-Piston Stirling Microcogeneration, IEEE Trans. Ind. Appl. 51 (2015) 3716–3733. https://doi.org/10.1109/TIA.2015.2427284.

[40] M. Majidniya, T. Boileau, B. Remy, M. Zandi, Nonlinear modeling of a Free Piston Stirling Engine combined with a Permanent Magnet Linear Synchronous Machine, Appl. Therm. Eng. 165 (2020) 114544. https://doi.org/10.1016/j.applthermaleng.2019.114544.

[41] M. Majidniya, T. Boileau, B. Remy, M. Zandi, Performance simulation by a nonlinear thermodynamic model for a Free Piston Stirling Engine with a linear generator, Appl. Therm. Eng. 184 (2021) 116128. https://doi.org/10.1016/j.applthermaleng.2020.116128.

[42] G. Brus, P.F. Raczkowski, M. Kishimoto, H. Iwai, J.S. Szmyd, A microstructure-oriented mathematical model of a direct internal reforming solid oxide fuel cell, Energy Convers. Manag. 213 (2020) 112826. https://doi.org/10.1016/j.enconman.2020.112826.

[43] P. Costamagna, K. Honegger, Modeling of Solid Oxide Heat Exchanger Integrated Stacks and Simulation at High Fuel Utilization, J. Electrochem. Soc. 145 (1998) 3995–4007. https://doi.org/10.1149/1.1838904.

[44] C.O. Colpan, I. Dincer, F. Hamdullahpur, Thermodynamic modeling of direct internal reforming solid oxide fuel cells operating with syngas, Int. J. Hydrogen Energy. 32 (2007) 787–795. https://doi.org/10.1016/j.ijhydene.2006.10.059.

[45] S. Motahar, A.A. Alemrajabi, Exergy based performance analysis of a solid oxide fuel cell and steam injected gas turbine hybrid power system, Int. J. Hydrogen Energy. 34 (2009) 2396–2407. https://doi.org/10.1016/j.ijhydene.2008.12.065.

[46] A. Arsalis, M.R. Von Spakovsky, F. Calise, Thermoeconomic modeling and parametric study of hybrid solid oxide fuel cell-gas turbine-steam turbine power plants ranging from 1.5 MWe to 10 MWe, J. Fuel Cell Sci. Technol. 6 (2009) 0110151–01101512. https://doi.org/10.1115/1.2971127.

[47] F. Calise, M. Dentice d'Accadia, A. Palombo, L. Vanoli, Simulation and exergy analysis of a hybrid Solid Oxide Fuel Cell (SOFC)-Gas Turbine System, Energy. 31 (2006) 3278–3299. https://doi.org/10.1016/j.energy.2006.03.006.

[48] S.H. Chan, K.A. Khor, Z.T. Xia, Complete polarization model of a solid oxide fuel cell and its sensitivity to the change of cell component thickness, J. Power Sources. 93 (2001) 130–140. https://doi.org/10.1016/S0378-7753(00)00556-5.

[49] J. Pirkandi, M. Ghassemi, M.H. Hamedi, R. Mohammadi, Electrochemical and thermodynamic modeling of a CHP system using tubular solid oxide fuel cell (SOFC-CHP), J. Clean. Prod. 29–30 (2012) 151–162. https://doi.org/10.1016/j.jclepro.2012.01.038.

[50] W. Ye, P. Yang, Y. Liu, Multi-objective thermodynamic optimization of a free piston Stirling engine using response surface methodology, Energy Convers. Manag. 176 (2018) 147–163. https://doi.org/10.1016/j.enconman.2018.09.011.

[51] J. Schreiber, TESTING AND PERFORMANCE CHARACTERISTICS OF A 1-kW FREE PISTON STIRLING ENGINE., NASA Tech. Memo. (1983).

[52] L.A. McNeely, Thermodynamic Properties of Aqueous Solutions of Lithium Bromide., ASHRAE Trans. 85 (1979) 413–434.

[53] B.H. Gebreslassie, M. Medrano, D. Boer, Exergy analysis of multi-effect water-LiBr absorption systems: From half to triple effect, Renew. Energy. 35 (2010) 1773–1782. https://doi.org/10.1016/j.renene.2010.01.009.